



Communication

Detection and Analysis of Airport Tailwind Events Triggered by Frontal Activity

Yue Liu¹, Yixiang Chen ¹, Jinlong Yuan ^{1,2,3},*, Zhekai Li¹, Fangzhi Wei¹, Tianwen Wei¹, Jiadong Hu ^{1,4} and Haiyun Xia ^{1,2,4,5}

- School of Atmospheric Physics, Nanjing University of Information Science and Technology, Nanjing 210044, China; 202412051911@nuist.edu.cn (Y.L.); 202411050001@nuist.edu.cn (Y.C.); 202412051912@nuist.edu.cn (Z.L.); 202412030260@nuist.edu.cn (F.W.); twwei@nuist.edu.cn (T.W.); hujd0707@nuist.edu.cn (J.H.); hsia@ustc.edu.cn (H.X.)
- State Key Laboratory of Climate System Prediction and Risk Management, Nanjing University of Information Science and Technology, Nanjing 210044, China
- Weather Modification Centre, China Meteorological Administration, Beijing 100081, China
- ⁴ Institute of Lidar Technology, GuangZai Co., Ltd., Hangzhou 310005, China
- School of Earth and Space Science, University of Science and Technology of China, Hefei 230026, China
- * Correspondence: yuanjinlong@nuist.edu.cn

Highlights

What are the main findings?

- This study integrates coherent Doppler wind lidar (CDWL) and ERA5 reanalysis data, revealing that frontal activity plus Taihang Mountains' topographic constraints drives excessive tailwinds at Beijing Daxing International Airport.
- CDWL captures fine low-level wind field variation, with its data consistent with ERA5 in time and space, verifying multi-source data reliability for tailwind research.

What is the implication of the main finding?

- The revealed tailwind triggering mechanism may provide a basis for airport operation optimization, contributing to improved aviation safety.
- The CDWL and ERA5 analytical framework is applicable to tailwind studies at other airports, providing a reference for tailwind events triggered by diverse climates and topography.

Abstract

Excessive tailwind, threatening the safety of aircraft takeoff and landing, is one of the prominent research topics in the field of aviation meteorology. This paper analyzes the causes of tailwinds at Beijing Daxing International Airport (BDIA), based on coherent Doppler wind lidar (CDWL) and ERA5 reanalysis data. CDWL with high spatiotemporal resolution is utilized to detect variations in the low-level wind field in the vicinity of airport areas. ERA5 reanalysis data are employed to investigate the distribution characteristics of meteorological elements such as wind fields, pressure, and temperature in the Beijing surrounding regions. The study of two typical tailwind events reveals that frontal activity, through the combined effects of pressure gradient adjustment and topographic constraints from the Taihang Mountains, drives the development of low-level southerly jets. It serves as the key mechanism triggering excessive tailwind. By integrating CDWL and ERA5 data for local and regional analysis, this study contributes to enhancing understanding of tailwind causal mechanisms and provides critical support for aviation meteorological disaster early warning.



Academic Editor: Stephan Havemann

Received: 19 July 2025 Revised: 29 August 2025 Accepted: 5 September 2025 Published: 9 September 2025

Citation: Liu, Y.; Chen, Y.; Yuan, J.; Li, Z.; Wei, F.; Wei, T.; Hu, J.; Xia, H.

Detection and Analysis of Airport
Tailwind Events Triggered by Frontal
Activity. *Remote Sens.* 2025, 17, 3127.

https://doi.org/10.3390/rs17183127

Copyright: © 2025 by the authors. Licensee MDPI, Basel, Switzerland. This article is an open access article distributed under the terms and conditions of the Creative Commons Attribution (CC BY) license (https://creativecommons.org/licenses/by/4.0/).

Remote Sens. 2025, 17, 3127 2 of 10

Keywords: tailwind; coherent Doppler wind lidar; frontal activity; aviation safety

1. Introduction

With the development of the civil aviation industry, airport throughput has been continuously increasing, and the importance of aviation safety has become increasingly prominent. As a key meteorological factor affecting the takeoff and landing safety of aircraft, abnormal changes and extreme events in the low-level wind field can directly threaten aviation safety. Currently, airport wind field research mainly focuses on typical risk factors such as wind shear, turbulence, tailwind, crosswind, etc. [1–3]. Through multi-source monitoring means like surface meteorological stations, Doppler weather radars, wind profile radars and coherent Doppler wind lidars (CDWL), a relatively mature warning system and analytical methods for causal mechanisms have been established [4–8]. Although tailwind events do not receive as much attention as wind shear, they occur from time to time due to factors such as local circulation, terrain shielding, and seasonal wind field changes. From the perspective of aviation safety, strong tailwinds can cause changes in the airspeed of aircraft, disrupt the lift balance, and lead to an extended landing roll distance, thereby posing safety risks such as go-arounds and flight diversions. For example, at Hong Kong International Airport, two aircraft failed their approaches and diverted to Macau International Airport due to the strong tailwinds accompanied by thunderstorms [9]. In terms of airport operational efficiency, excessive tailwinds can trigger unfavorable runway configuration switches, significantly reduce airport capacity, and result in flight delays [10]. The existing studies primarily focus on the operational impacts of tailwinds, with few exploring the triggering mechanisms, such as the role of synoptic systems and local topography, on tailwind formation. Tailwind limits at airports vary in specific values due to factors such as runway characteristics (e.g., length, surface friction), aircraft performance (e.g., weight, wing configuration), and operational preferences, but generally do not exceed 10 knots (5 m/s) [11].

In recent years, CDWL has gradually emerged as a key tool for wind field monitoring at airports, leveraging its advantages of compact size, high spatiotemporal resolution, and robust anti-interference capability [12,13]. Airports such as Hong Kong International Airport [14], Narita International Airport [15], Lanzhou Zhongchuan Airport [16], and Beijing Capital International Airport [17] have all conducted wind shear detection experiments using CDWL. However, there are few studies on tailwind events based on CDWL.

Beijing Daxing International Airport (BDIA) is one of the world's largest single-terminal airports; it recorded a cumulative passenger throughput of 150 million at the end of January 2025. Located in the transition zone between the North China Plain and the Taihang Mountains, BDIA's low-level wind field is influenced by both mesoscale weather systems and local topography. Frontal activity, as one of the most typical weather systems in mid-latitudes, usually accompanied by temperature gradients, abrupt humidity changes, and drastic wind field variations, affects local convective activity and precipitation distribution [18]. Additionally, it directly disturbs the surface wind field through processes such as frontal zone movement and momentum downward transport [19], serving as a key factor triggering tailwinds. Thus, the triggering mechanism of such weather systems on local tailwind events in airports is worth studying.

This study, based on the experiments conducted by CDWL at BDIA, combined with ERA5 reanalysis data, systematically analyzes two typical tailwind events triggered by frontal activity in 2021. The paper is structured as follows: Section 2 describes the sources of experimental data; Section 3 analyzes the causes of the two events from the perspectives

Remote Sens. 2025, 17, 3127 3 of 10

of dynamic mechanisms and thermal conditions, combined with topographic analysis. Finally, a conclusion is drawn in Section 4. If not specified, UTC time is used.

2. Data and Materials

2.1. Site and Instruments

The experiment was conducted at BDIA, China (39°29'N, 116°24'E). BDIA is located in the northwest corner of the North China Plain, with terrain that gently slopes from west to southeast. The region is characterized by prevailing southwesterly winds throughout the year, with the wind direction exhibiting regional and seasonal variations. The airport features four runways, as shown in Figure 1b, with designations of 17R/35L, 17L/35R, 11L/29R, and 01L/19R. Among these, the north-south-oriented runways (17R/35L, 17L/35R, and 01L/19R) are the focus of these tailwind analyses. The CDWL employed in this experiment, as shown in Figure 1c, was installed at the location marked by the red circle. It operates at an eye-safe wavelength of 1.5 μm, with each beam featuring a spatial resolution of 30 m and a temporal resolution of 0.2 s. The system employs a plan position indicator (PPI) scanning mode with a period of approximately 40 s. The azimuth angle scanning range is set to 150–360°, which is specifically designed to fully cover the critical airspace for takeoff and landing of BDIA's main operational north-south runway; this design also saves scanning time. The elevation angle ranges from 0° to 7° [20]. During the experiment, the flight crew reported sixteen tailwind exceedance events, and this study selected two of these cases for analysis.

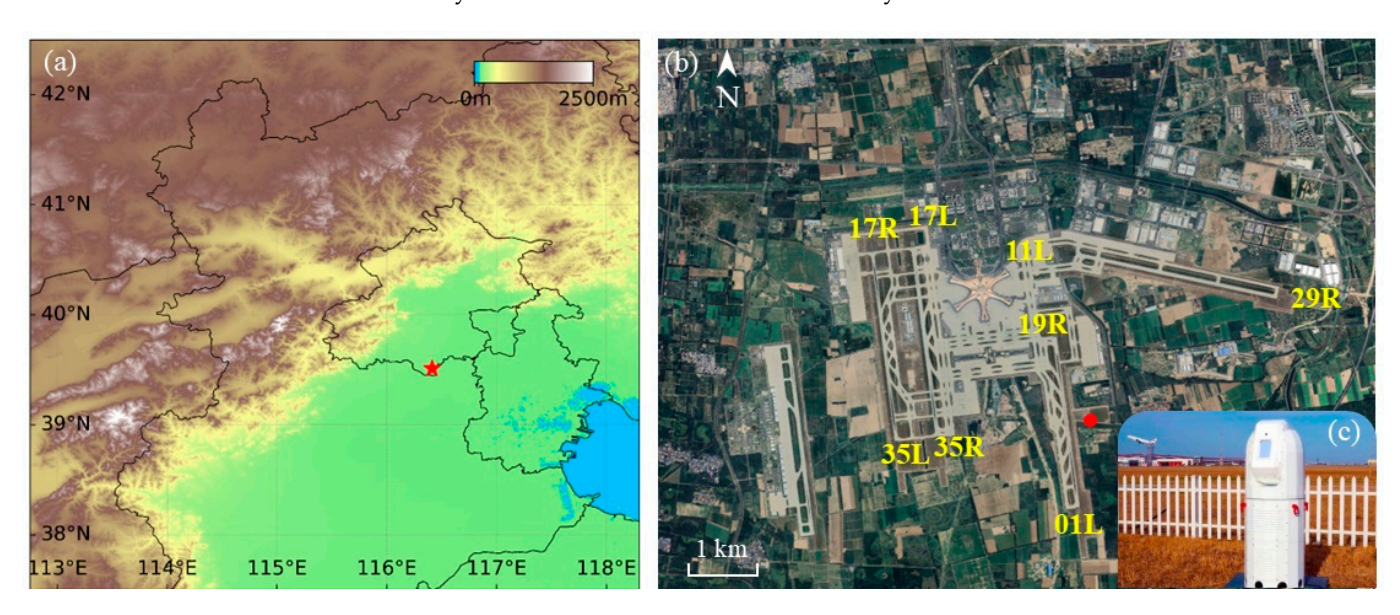


Figure 1. (a) Topographic map of the transition zone between the North China Plain and the Taihang Mountains, the red five-pointed star marking the location of BDIA. (b) The runway layout of BDIA, the red circle marking the location of CDWL. (c) Photograph of the CDWL.

2.2. ERA5 Reanalysis Data

The ERA5 dataset, provided by the European Centre for Medium-Range Weather Forecasts (ECMWF), is a global meteorological reanalysis dataset. It is generated using advanced numerical weather prediction techniques, based on extensive observational data and numerical weather prediction models. The ERA5 dataset has a spatial resolution of $0.25^{\circ} \times 0.25^{\circ}$ and an hourly temporal resolution. It covers multi-level atmospheric data from the surface to high altitudes. A series of previous studies have already conducted investigations into the usability of ERA5 reanalysis data; furthermore, ERA5 reanalysis data is often used as a reference for evaluating the accuracy of observational data from

Remote Sens. 2025, 17, 3127 4 of 10

radars [21–23]. This study selected reanalysis data covering the periods of 28 May 2021 and 1 July 2021, which incorporates meteorological elements such as horizontal wind fields, temperature, humidity, and geopotential height, aiming to analyze the dynamic and thermal causes of tailwind events.

3. Typical Excessive Tailwind Event

3.1. Tailwind Triggered by a Warm Front

Figure 2 shows the 3° elevation PPI scanning results from CDWL on 28 May 2021. At 11:40:37, BDIA is under a stable south wind of 5 m/s, with wind directions concentrated at $180^\circ \pm 3^\circ$. Horizontal wind speeds exhibited uniform distribution with relatively low windshear. One hour later, the south wind field persisted, and wind speeds increased to 10 m/s. At 13:40:02, the mean wind speed had exceeded 12 m/s, significantly surpassing the safety threshold of 10 kt. If an aircraft takes off or lands northward on a north–south runway under such conditions, it will encounter a severe excessive tailwind event.

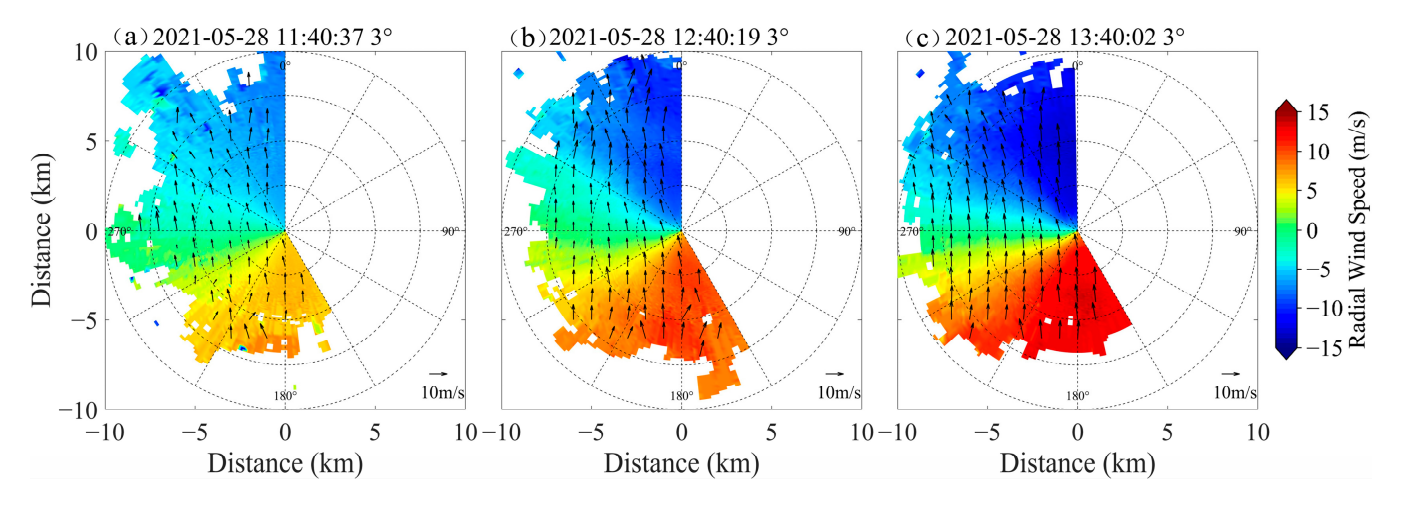


Figure 2. (a–c) show the detection results of the CDWL in PPI scan mode at a 3° elevation angle, recorded at different times on 28 May 2021, the arrows showing the two-dimensionally decomposed wind field derived from radial wind velocity.

The hourly wind speed evolution characteristics in the near-surface layer of BDIA are clearly captured in the 975 hPa wind field, as shown in Figure 3a–c. From 12:00 to 14:00, the airport remained in a southerly wind field. As the high-wind-speed area southwest of the airport expanded northward, the wind speed at the airport increased steadily. At 12:00, the wind speed was approximately 6 m/s; one hour later, it increased to 8 m/s, and by 14:00, it exceeded 10 m/s. This exhibited high consistency in temporal sequence and spatial extent with the near-surface high-wind-speed zones recorded in the results from the CDWL, verifying the reliability of the lidar data. Figure 3d–f present the vertical cross-section of horizontal wind speed along 116.25°E. From 12:00 to 14:00, horizontal wind speeds increased continuously in the 900–1000 hPa layer between 37°N and 40°N. At 13:00, a maximum horizontal wind speed of approximately 10 m/s appeared at 975 hPa. Over BDIA (39.25°N), the wind speed at the upper level of 800 hPa is 8 m/s. Moving downward to the 950–975 hPa layer, the wind speed gradually increases to 11 m/s. From 975 hPa further downward to 1000 hPa, the wind speed decreases again. This structure matches the vertical profile of a typical low-level jet.

To investigate the formation mechanism of the low-level jet, this study utilizes the evolution characteristics of equivalent potential temperature (θ_e) and geopotential height field to analyze the dynamic–thermal effects on airflow acceleration. As shown in Figure 4a–c, the distribution of θ_e forms a northwest–southeast-oriented dense band between 39°N and

Remote Sens. 2025, 17, 3127 5 of 10

44°N. In this band, the warm moist air mass surges into the dry cold region, showcasing a typical characteristic of a warm front zone. From 08:00 to 14:00 on 28 May, the warm front zone continuously shifts southeastward. The strong temperature–moisture contrast near the front provides thermodynamic conditions for the release of unstable energy and airflow acceleration. The geopotential height field exhibits a typical configuration with lower values in the north and higher values in the south. Tracking the evolution of contour lines at consecutive 3 h intervals reveals that the low-pressure system moves southeastward, with its dense contour zone extending synchronously southeastward. This results in a significant enhancement of the pressure gradient between the two systems, directly driving airflow acceleration. Meanwhile, warm moist air ahead of the warm front further strengthens atmospheric baroclinicity through latent heat release, promoting the concentration and acceleration of airflow near the front zone and ultimately forming the low-level southerly jet.

Based on the conditions for jet formation provided by the dynamic–thermal processes, topographic effects are considered to further analyze their regulation of airflow. Figure 4d–f show the superimposed 925 hPa wind field and topographic map; the arrows indicate the actual airflow direction and speed at the 925 hPa level, with the orientation of the Taihang Mountains constraining the jet's flow direction. Against the synoptic system background shown in Figure 4a–c, the initial airflow at the 925 hPa level is driven by the pressure gradient force. Due to mountain barriers, the air flows along the eastern flank of the mountains, forming a pattern where airflow aligns closely with the mountain orientation from northern Henan to central Hebei. The wind direction is strictly confined to southerly–southwesterly directions. The mountains' continuous barrier effect further restricts lateral airflow diffusion. This causes concentrated transport along the mountain range toward Beijing, triggering an excessive tailwind event.

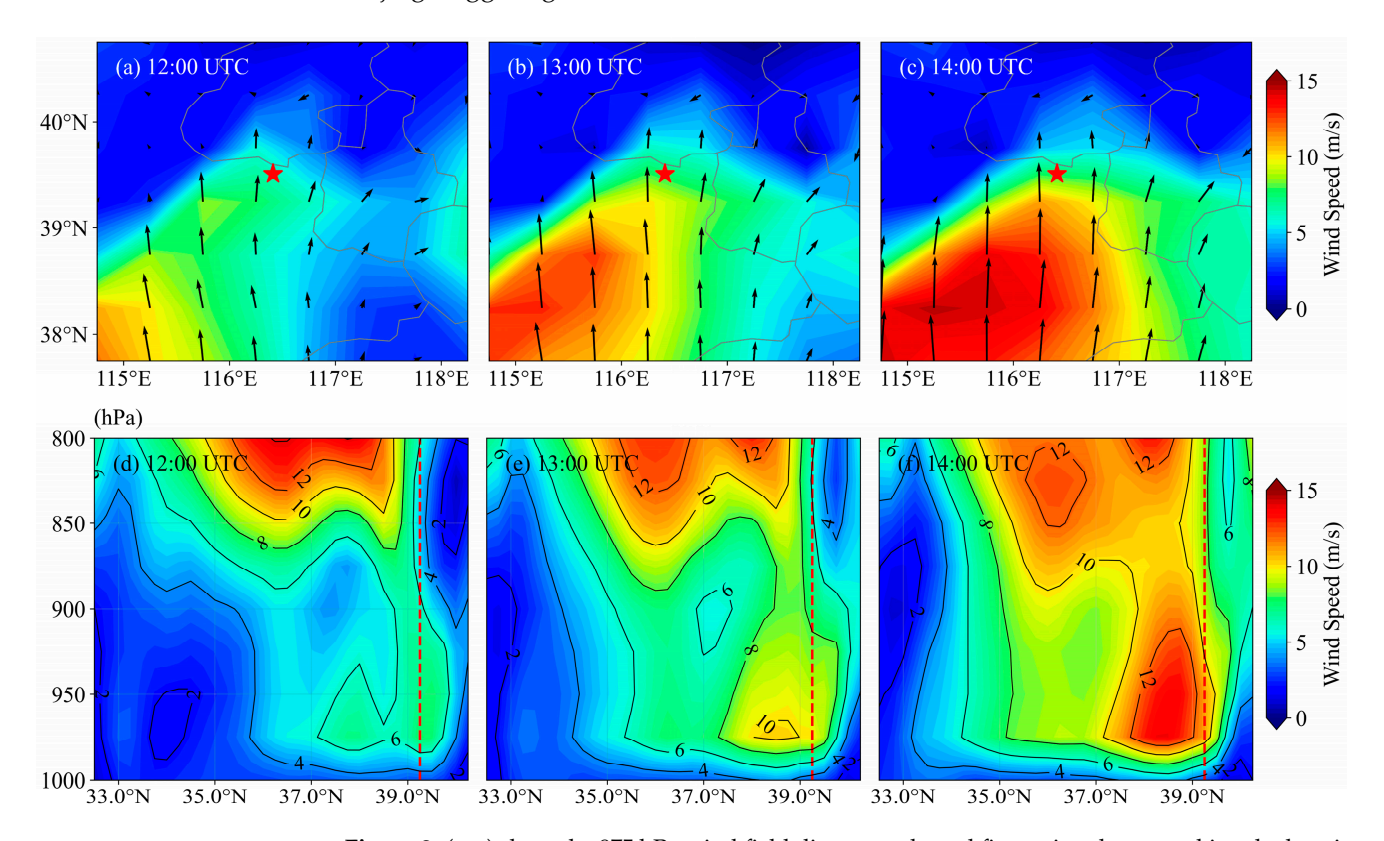


Figure 3. (**a–c**) show the 975 hPa wind field diagrams, the red five-pointed star marking the location of BDIA, the arrows indicating wind direction and speed; (**d–f**) show the horizontal wind speed diagrams of the vertical cross-section along 116.25°, the red dashed line indicating the latitude of BDIA.

Remote Sens. 2025, 17, 3127 6 of 10

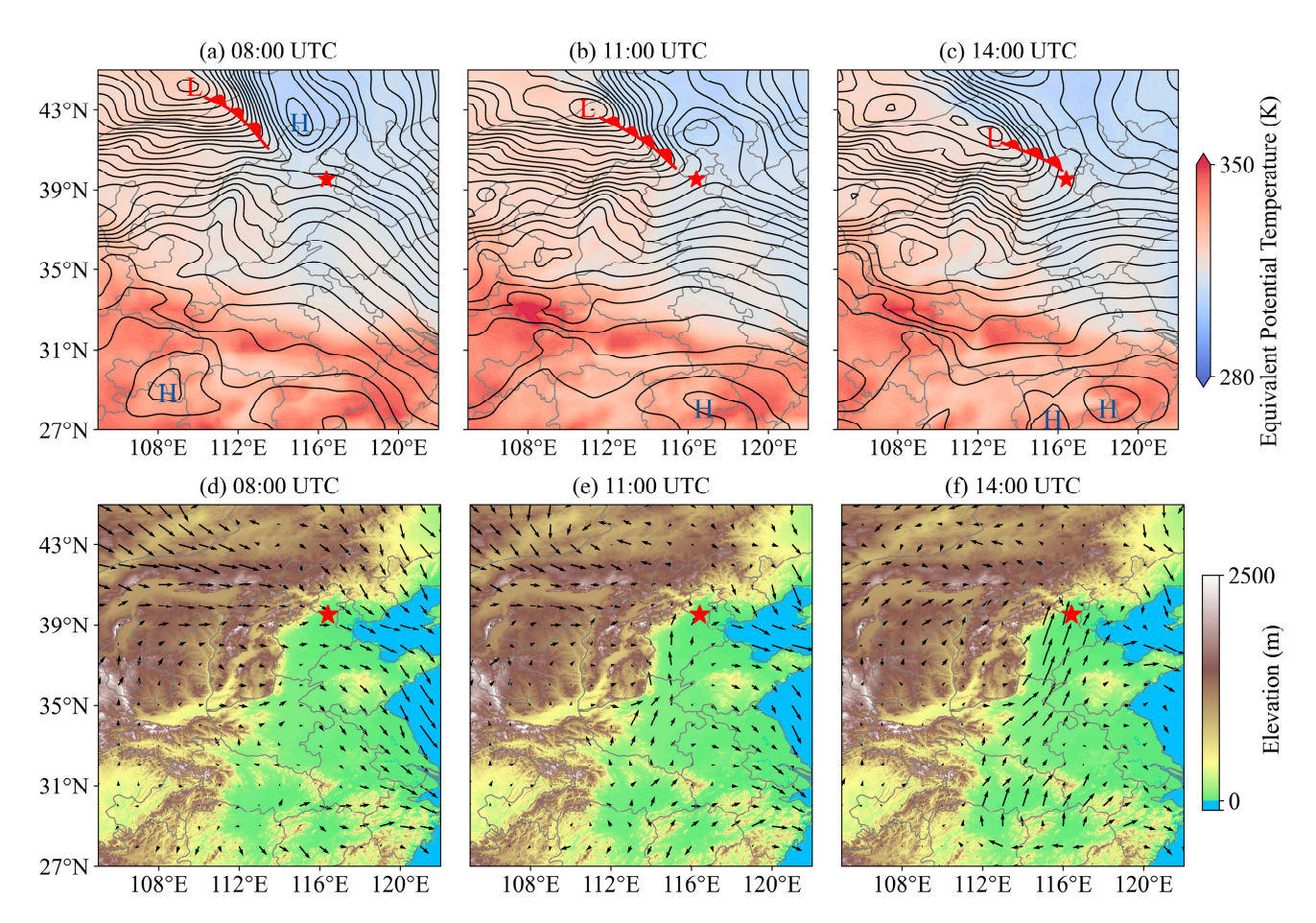


Figure 4. (a–c) show the 925 hPa equivalent potential temperature field and geopotential height contours, with the letter "L" denoting the low-pressure center, "H" denoting the high-pressure center, and the red warm front symbol denoting the position of the warm front; (d–f) show the topographic schematic of the Taihang Mountains west of BDIA overlaid with 925 hPa wind field, the red five-pointed star marking the location of BDIA and the arrows indicating wind direction and speed.

3.2. Tailwind Triggered by a Cold Front

Figure 5 shows the 3° elevation PPI scanning results from CDWL on 1 July 2021. At 02:58:20, BDIA experiences primarily westerly winds; the wind speeds show uneven distribution and remain relatively low. About two hours later, the wind direction shifts. Its distribution scatters and speeds increase slightly. At 07:06:20, the airport's wind direction transitions to southerly, concentrated within $180^\circ \pm 3^\circ$. Average wind speed exceeds 10 m/s, significantly surpassing the 10 kt safety threshold. Under such conditions, a northward takeoff or landing on a north–south runway would cause the aircraft to encounter an excessive tailwind event.

The 975 hPa wind field illustrates the hourly wind speed evolution characteristics in the near-surface layer of BDIA. As shown in Figure 6a–c, the airport was under a southwesterly wind field at 03:00. Subsequently, the wind direction shifted due southerly. From 05:00 to 07:00, both wind direction and speed remained stable, with wind speeds exceeding 8 m/s. Since ERA5 provides hourly averaged data, it shows slight discrepancies with the fine-scale wind field variations observed by CDWL, which has second-level resolution scanning. However, the two datasets exhibit consistent trends in wind field changes.

Remote Sens. 2025, 17, 3127 7 of 10

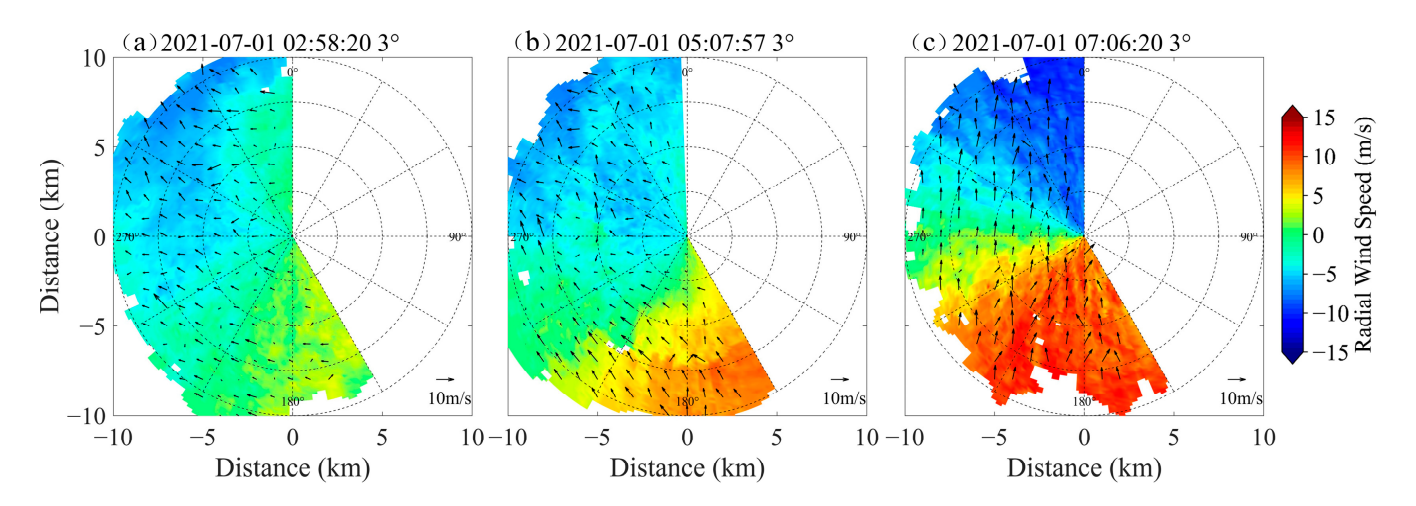


Figure 5. (a–c) show the detection results of the CDWL in PPI scan mode at a 3° elevation angle, recorded at different times on 1 July 2021, the arrows showing the two-dimensionally decomposed wind field derived from radial wind velocity.

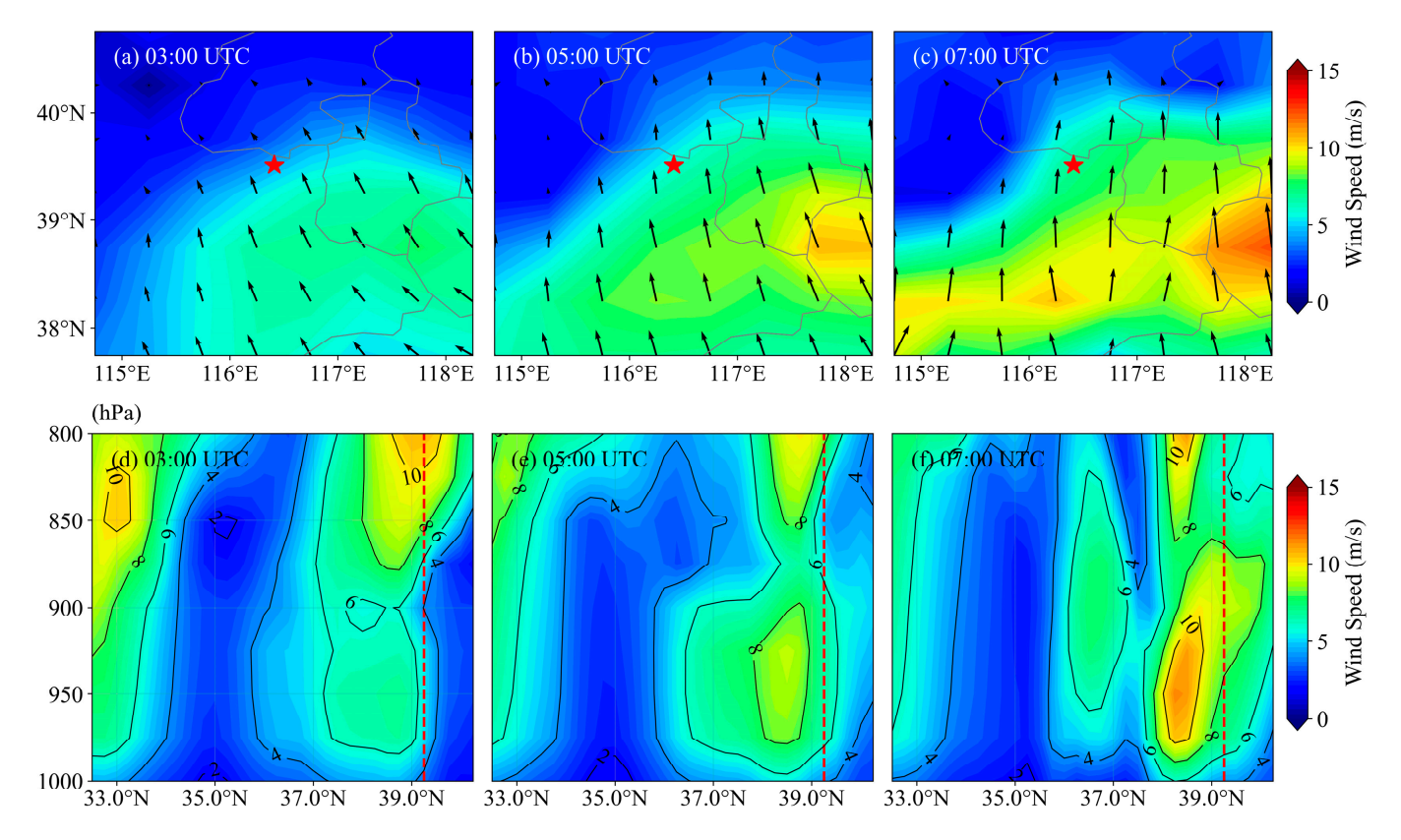


Figure 6. (**a–c**) show the 975 hPa wind field diagrams, the red five-pointed star marking the location of BDIA, the arrows indicating wind direction and speed; (**d–f**) show the horizontal wind speed diagrams of the vertical cross-section along 116.25°E, the red dashed line indicating the latitude of BDIA.

Figure 6d–f present the vertical cross-section of horizontal wind speed along 116.25°E. From 03:00 to 07:00, the upper-level wind speed decreases, while the lower-level horizontal wind speed increases continuously, and the high-speed zone shows a tendency to move northward. At 07:00, over BDIA (39.25°N), the wind speed at the upper level of 800 hPa is 7 m/s. Moving downward to the 950–975 hPa layer, the wind speed gradually increases and reaches 9 m/s. From 950 hPa further downward to 1000 hPa, the wind speed gradually decreases again. This structure matches the vertical profile of a typical low-level jet.

Remote Sens. 2025, 17, 3127 8 of 10

Similarly, to analyze the causes of this low-level jet, θ_e distribution and geopotential height field evolution were used to examine the dynamic–thermal effects on airflow acceleration. Figure 7a–c show the 925 hPa θ_e shaded map overlaid with geopotential height lines. From 02:00 to 08:00, analysis indicates this southerly excessive tailwind event was primarily triggered by the jet ahead of the cold front. Specifically, Figure 7a–c illustrate that θ_e presents a prominent high-value zone and a low-value zone, forming a distinct gradient band. This southwest–northeast-oriented dense band of gradient serves as the core indicator of the cold front, which remained stationary from 02:00 to 08:00. Such stability provided a consistent thermodynamic environment for energy accumulation within the warm sector and enhanced atmospheric baroclinicity. It also promoted convergence of warm moist airflow ahead of the front, accumulating energy for subsequent jet development. Concurrently, the intensification of the frontal zone caused the geopotential height lines to be compressed and converged, which supplied dynamic sources for airflow acceleration.

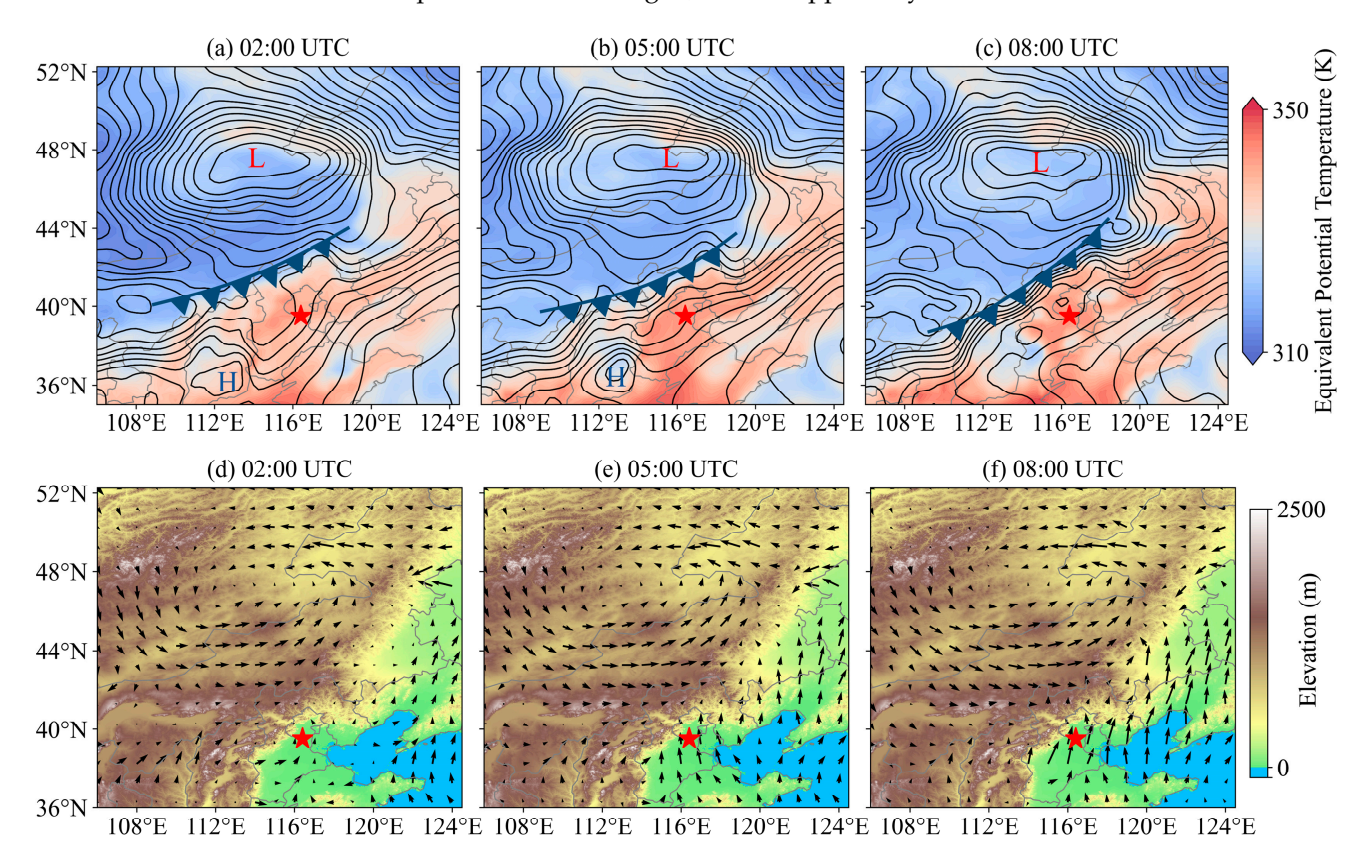


Figure 7. (a–c) show the 925 hPa equivalent potential temperature field and geopotential height contours, with the letter "L" denoting the low-pressure center, "H" denoting the high-pressure center, and the blue cold front symbol denoting the position of the cold front; (d–f) show the topographic schematic of the Taihang Mountains west of BDIA overlaid with 925 hPa wind field, the red five-pointed star marking the location of BDIA and the arrows indicating wind direction and speed.

In addition to these dynamic–thermal mechanisms, topographic factors further regulated the airflow path. Figure 7d–f illustrate that the Taihang Mountains west of Beijing are oriented in a northeast–southwest direction. Under the background of pre-frontal jet formation during 02:00 to 08:00, airflow driven by the pressure gradient was unable to directly cross the mountains. Instead, it was forced to flow along the eastern piedmont zone adjacent to the mountain range. The continuous barrier effect of the mountains restricted lateral diffusion of the southerly wind, compressing its path along the eastern mountain flank, from west Beijing to the airport vicinity. This topographic constraint further concentrated the airflow, ultimately leading to the excessive tailwind event.

Remote Sens. 2025, 17, 3127 9 of 10

4. Conclusions

Focusing on BDIA, the causal mechanisms of tailwind under frontal activity are investigated by integrating high-spatiotemporal-resolution wind field data from CDWL and ERA5 reanalysis data. The 28 May and 1 July 2021 events shared the same core drivers. Frontal zone dynamics involved warm- and cold-front-enhanced pressure gradients, while the Taihang Mountain topography constrained airflow paths to induce tailwind effects. Meanwhile, there were differences in their formation processes. On 28 May, warm front movement created strong temperature–moisture gradients, which thermodynamically accelerated airflow. Southeastward-moving low-pressure systems strengthened the pressure gradient. These factors drove a low-level southerly jet. The 1 July event, in contrast, resulted from cold front intensification and passive pressure gradient enhancement. This combination sustained the growth of pre-frontal southerly winds.

By integrating CDWL local monitoring with ERA5 regional system analysis, the study reveals that CDWL data precisely captured the wind field evolution. ERA5 reanalysis data clarified the regional synoptic background of tailwinds from thermodynamic, dynamic, and vertical structural perspectives. The high consistency between ERA5 data and CDWL in temporal sequence and spatial extent validates the reliability of multi-source data collaborative analysis. This work establishes a technical paradigm for short-term tailwind analysis. It provides references for optimizing airport operations such as dynamically adjusting runway directions and issuing advance tailwind warnings during frontal activity. The analysis framework combining ERA5 and CDWL data is applicable to tailwind event studies at other airports, but specific triggering mechanisms may vary due to differences in topography and climate. Future research may further expand to other meteorological drivers and diverse topographic settings, integrate multi-source observation data, and optimize tailwind warning models to improve applicability in complex environments.

Author Contributions: Conceptualization, J.Y.; Methodology, Y.L.; Software, Y.L. and Y.C.; Formal Analysis, J.Y. and Y.L.; Investigation, Y.L.; Resources, J.Y.; Data Curation, J.Y.; Writing—Original Draft Preparation, Y.L. and J.Y.; Writing—Review and Editing, Z.L., F.W., T.W., J.H. and H.X.; Visualization, Y.L.; Supervision, J.Y. All authors have read and agreed to the published version of the manuscript.

Funding: This work was financially supported by the National Natural Science Foundation of China (42405137), the Natural Science Foundation of Jiangsu Province (No. BK20230434) and the Aeronautical Science Foundation of China (No. 202300220R2001).

Data Availability Statement: Data underlying the results presented in this paper can be obtained from the authors upon reasonable request.

Acknowledgments: We express gratitude to BDIA for supplying flight crew reports. We acknowledge the contributions of Hao Huang, Wei Zhong and Xi Zhang to the field experiment.

Conflicts of Interest: Author Jinlong Yuan was employed by the company GuangZai Co., Ltd. The remaining authors declare that the research was conducted in the absence of any commercial or financial relationships that could be construed as a potential conflict of interest.

References

- 1. Chan, P.W. A Significant Wind Shear Event Leading to Aircraft Diversion at the Hong Kong International Airport. *Meteorol. Appl.* **2012**, 19, 10–16. [CrossRef]
- Chan, P.W.; Leung, Y.Y.; Lai, K.K. A Meteorological Analysis of the Missed Approach of an Aircraft at Taoyuan International Airport, Taiwan, During Typhoon Kong-Rey in 2024—The Impact of Crosswind and Turbulence. *Atmosphere* 2025, 16, 660.
 [CrossRef]
- 3. Huang, X.; Zheng, J.; Shao, A.; Xu, D.; Tian, W.; Li, J. Study of Low-Level Wind Shear at a Qinghai-Tibetan Plateau Airport. *Atmos. Res.* 2024, 311, 107680. [CrossRef]

Remote Sens. 2025, 17, 3127

4. Chan, P.W. LIDAR-Based Turbulence Intensity Calculation Using Glide-Path Scans of the Doppler Light Detection and Ranging (LIDAR) Systems at the Hong Kong International Airport and Comparison with Flight Data and a Turbulence Alerting System. *Meteorol. Z.* **2010**, *19*, 549–563. [CrossRef]

- 5. Chan, P.W.; Hon, K.K.; Shin, D.K. Combined Use of Headwind Ramps and Gradients Based on LIDAR Data in the Alerting of Low-Level Windshear/Turbulence. *Meteorol. Z.* **2011**, *20*, 661–670. [CrossRef] [PubMed]
- 6. Wu, T.-C.; Hon, K.-K. Application of Spectral Decomposition of LIDAR-Based Headwind Profiles in Windshear Detection at the Hong Kong International Airport. *Meteorol. Z.* **2018**, 27, 33–42. [CrossRef]
- 7. O' Connor, A.; Kearney, D. Low Level Turbulence Detection for Airports. Int. J. Aviat. Aeronaut. Aerosp. 2019, 6, 3. [CrossRef]
- 8. Nechaj, P.; Gaál, L.; Bartok, J.; Vorobyeva, O.; Gera, M.; Kelemen, M.; Polishchuk, V. Monitoring of Low-Level Wind Shear by Ground-Based 3D Lidar for Increased Flight Safety, Protection of Human Lives and Health. *Int. J. Environ. Res. Public Health* **2019**, *16*, 4584. [CrossRef]
- 9. Tse, S.M.; Chan, P.W.; Wong, W.K. A Case Study of Missed Approach of Aircraft Due to Tailwind Associated with Thunderstorms. *Meteorol. Appl.* **2014**, 21, 50–61. [CrossRef]
- 10. Maslovara, A.; Mirković, B. Impact of Tailwind on Airport Capacity and Delay at Zurich Airport. *Transp. Res. Procedia* **2021**, *59*, 117–126. [CrossRef]
- 11. Hord, C. The Provision of Crosswind and Tailwind Information. In Proceedings of the Aerodrome Meteorological Observation and Forecast Study Group (AMOFSG) Tenth Meeting, Montreal, QC, Canada, 17–19 June 2013.
- 12. Liu, Z.; Barlow, J.F.; Chan, P.-W.; Fung, J.C.H.; Li, Y.; Ren, C.; Mak, H.W.L.; Ng, E. A Review of Progress and Applications of Pulsed Doppler Wind LiDARs. *Remote Sens.* **2019**, *11*, 2522. [CrossRef]
- 13. Xia, H.; Chen, Y.; Yuan, J.; Su, L.; Yuan, Z.; Huang, S.; Zhao, D. Windshear Detection in Rain Using a 30 Km Radius Coherent Doppler Wind Lidar at Mega Airport in Plateau. *Remote Sens.* **2024**, *16*, 924. [CrossRef]
- 14. Hon, K.K.; Chan, P.W.; Chiu, Y.Y.; Tang, W. Application of Short-Range LIDAR in Early Alerting for Low-Level Windshear and Turbulence at Hong Kong International Airport. *Adv. Meteorol.* **2014**, 2014, 162748. [CrossRef]
- 15. Yoshino, K. Low-Level Wind Shear Induced by Horizontal Roll Vortices at Narita International Airport, Japan. *J. Meteorol. Soc. Jpn. II* **2019**, 97, 403–421. [CrossRef]
- 16. Li, L.; Shao, A.; Zhang, K.; Ding, N.; Chan, P.-W. Low-Level Wind Shear Characteristics and Lidar-Based Alerting at Lanzhou Zhongchuan International Airport, China. *J. Meteorol. Res.* **2020**, *34*, 633–645. [CrossRef]
- 17. Zhang, H.; Wu, S.; Wang, Q.; Liu, B.; Zhai, X. Airport Low-Level Wind Shear Lidar Observation at Beijing Capital International Airport. *EPJ Web Conf.* **2018**, *176*, 06013. [CrossRef]
- 18. Li, Y.; Wang, Y.; Chen, X. The Influence of a Cold Front and Topography on the Initiation and Maintenance of a Precipitation Convective System in North China: A Case Study. *Int. J. Environ. Res. Public Health* **2022**, *19*, 9484. [CrossRef]
- 19. Zhao, S.; Yang, C.; Shan, Y.; Zhu, F. Identification and Analysis of Wind Shear Within the Transiting Frontal System at Xining International Airport Using Lidar. *Remote Sens.* **2025**, *17*, 732. [CrossRef]
- 20. Yuan, J.; Su, L.; Xia, H.; Li, Y.; Zhang, M.; Zhen, G.; Li, J. Microburst, Windshear, Gust Front, and Vortex Detection in Mega Airport Using a Single Coherent Doppler Wind Lidar. *Remote Sens.* **2022**, *14*, 1626. [CrossRef]
- 21. Deng, X.; He, D.; Zhang, G.; Zhu, S.; Dai, R.; Jin, X.; Fu, W.; Shen, W.; Chen, J.; Fan, Y.; et al. Comparison of Horizontal Wind Observed by Wind Profiler Radars with ERA5 Reanalysis Data in Anhui, China. *Theor. Appl. Climatol.* **2022**, 150, 1745–1760. [CrossRef]
- 22. Yu, J.; Zhou, T.; Jiang, Z.; Zou, L. Evaluation of Near-Surface Wind Speed Changes During 1979 to 2011 over China Based on Five Reanalysis Datasets. *Atmosphere* 2019, 10, 804. [CrossRef]
- Wei, Y.; Peng, K.; Ma, Y.; Sun, Y.; Zhao, D.; Ren, X.; Yang, S.; Ahmad, M.; Pan, X.; Wang, Z.; et al. Validation of ERA5 Boundary Layer Meteorological Variables by Remote-Sensing Measurements in the Southeast China Mountains. Remote Sens. 2024, 16, 548.
 [CrossRef]

Disclaimer/Publisher's Note: The statements, opinions and data contained in all publications are solely those of the individual author(s) and contributor(s) and not of MDPI and/or the editor(s). MDPI and/or the editor(s) disclaim responsibility for any injury to people or property resulting from any ideas, methods, instructions or products referred to in the content.